Bidirectional RO-ISAC Based on Clipped mCAP: Subband Division Duplexing and Unified Performance Metric Design

Yungui Nie, Chen Chen, *Senior Member, IEEE,* Zhihong Zeng, Xiaodi You, Harald Haas, *Fellow, IEEE,* and Gangxiang Shen, *Senior Member, IEEE, Fellow, Optica*

***Abstract*—Driven by the sensing potential of optical signals, optical integrated sensing and communication (O-ISAC) is becoming a major research focus, especially the development of retroreflective optical ISAC (RO-ISAC) through the use of corner cube reflector (CCR). This paper proposes a novel bidirectional RO-ISAC system based on clipped multi-band carrierless amplitude and phase (mCAP), which utilizes subband division duplexing (SDD) to assign different frequency subbands to the downlink and uplink. Under this architecture, the downlink reflected signal and the uplink signal share the same photodetector (PD), leading to asynchronous superposition in the time domain. While the uplink communication signal can be successfully recovered from the mixture by leveraging the matched filtering capability of mCAP, the downlink sensing process remains compromised by uplink interference. To mitigate the interference of the uplink signal on the reflected downlink signal, we propose an interference cancellation method to enhance sensing accuracy, thereby enabling simultaneous downlink communication and sensing. By adjusting the clipping ratio (CR), a trade-off between downlink communication and sensing performance is achieved, while the bit error rate (BER) performance of the uplink is simultaneously optimized. Moreover, to jointly optimize downlink communication and sensing performance, we further propose a unified performance metric called the joint communication-sensing outage probability (JCSOP). Extensive experimental results are presented to demonstrate the feasibility of the proposed bidirectional RO-ISAC system based on clipped mCAP.**

***Index Terms*—retroreflective optical integrated sensing and communication (RO-ISAC), carrierless amplitude and phase modulation, subband division duplexing, interference cancellation.**

I. Introduction

THROUGH deep integration with various industries, the sixth-generation (6G) mobile communication drives the evolution of network architecture from single-functionality to multi-functionality [1]. This process not only requires satisfying ultra-high data rates and low latency but also supporting efficient human-machine-thing intelligent interconnection, which places stricter demands on overall system capabilities. In this context, integrated sensing and communication (ISAC) serves as a core technology to meet this comprehensive demand by providing intelligent services through multi-functional integration [2], [3], [4]. Although ISAC has achieved significant progress in the radio frequency (RF) domain, the RF spectrum is becoming increasingly congested. Due to its advantages such as abundant unlicensed spectrum, optical wireless communication (OWC) serves as a vital complement [5]. By exploiting the sensing potential of optical signals, the concept of optical ISAC (O-ISAC) has emerged, attracting significant research interest [6], [7]. Recently, retroreflective optical ISAC (RO-ISAC) has been further studied [8], [9]. Compared with conventional ISAC, RO-ISAC enhances echo strength and sensing reliability by employing a retroreflective module to reflect the incident optical signal back to the transceiver, thus supporting joint communication and sensing [10]. Moreover, compared with diffuse and specular reflections, a passive corner cube reflector (CCR) is used to provide stronger, more stable echoes for reliable sensing.

The core essence of RO-ISAC lies in achieving efficient synergy and mutual benefit between communication and sensing, which not only promotes the significant enhancement of sensing capabilities but also offers new possibilities for the intelligent development of communication networks. By combining retroreflectors with ISAC technology, RO-ISAC can efficiently adapt to diverse application scenarios, such as unmanned aerial vehicle (UAV) [11] and Internet of Things (IoT) [12], [13]. The adopted ISAC waveform has a significant impact on the overall performance of the RO-ISAC system. Waveform design must simultaneously satisfy the dual requirements of communication and sensing, ensuring efficient and reliable information transmission while providing favorable signal characteristics for sensing tasks such as target detection and localization. At present, various waveform design schemes have been developed to balance the requirements of communication and sensing. Orthogonal time-frequency space (OTFS) [14] and affine frequency division multiplexing (AFDM) [15]

This work was supported by the National Natural Science Foundation of China under Grants W2411058, 62271091, 62501088 and 62001319, the Suzhou Science and Technology Bureau-Technical Innovation Project in Key Industries under Grant SYG202112, and the Open Fund of IPOC (BUPT) under Grant IPOC2020A009. *(Corresponding authors: Chen Chen; Gangxiang Shen)*

Yungui Nie, Xiaodi You and Gangxiang Shen are with the Jiangsu New Optical Fiber Technology and Communication Network Engineering Research Center, Suzhou Key Laboratory of Advanced Optical Communication Network Technology, Institute for Broadband Research & Innovation (IBRI) and School of Electronic and Information Engineering, Soochow University, Suzhou, Jiangsu 215006, China (e-mail: 20234028002@stu.suda.edu.cn; xdyou@suda.edu.cn; shengx@suda.edu.cn).

Chen Chen and Zhihong Zeng are with the School of Microelectronics and Communication Engineering, Chongqing University, Chongqing 400044, China (e-mail: c.chen@cqu.edu.cn; zhihong.zeng@cqu.edu.cn).

Harald Haas is with the Department of Engineering, University of Cambridge, 9 JJ Thomson Avenue, Cambridge CB3 0FA, UK (e-mail: huh21@cam.ac.uk).

have been widely studied in high-mobility ISAC systems, whereas optical ISAC requires dedicated waveform design due to its distinct channel characteristics. A hybrid waveform consisting of both pulse amplitude modulation (PAM) and orthogonal frequency division multiplexing (OFDM) samples was proposed to enable a flexible trade-off between communication and sensing performance [16]. To further improve sensing performance, a flexible waveform design based on OFDM-embedded maximum length sequence (OFDM-MLS) was proposed, leveraging both the exceptional sensing precision of MLS and the established communication reliability of OFDM [17]. To facilitate simultaneous communication and sensing for multiple users, a new OFDM-MLS with code index modulation (OFDM-MLS-CIM) waveform was proposed [18]. The above schemes predominantly adopt OFDM as the communication waveform. Moreover, clipped OFDM is employed in [19] to simultaneously enable communication and sensing. However, OFDM suffers from a high peak-to-average power ratio (PAPR), making it sensitive to system nonlinearities [20], [21]. Clipped OFDM is a practical solution to reduce PAPR by deliberately limiting the signal amplitude [22]. In addition, single-carrier waveform techniques with low PAPR characteristics, such as carrierless amplitude and phase modulation (CAP) [23], [24] have attracted increasing attention. By dividing the bandwidth into multiple subbands, CAP can be extended to multi-band CAP (mCAP) [25], [26], which is regarded as a multicarrier modulation technique. Although mCAP has been extensively studied in VLC systems that only consider communication [27], [28], its application in RO-ISAC systems has not yet been investigated.

To enable efficient information exchange between the transceiver and the target, RO-ISAC systems typically adopt a bidirectional link architecture. However, such an architecture faces severe bidirectional transmission interference, which necessitates the design of effective interference cancellation schemes to ensure reliable bidirectional communication and sensing. So far, several interference cancellation schemes have been proposed to mitigate bidirectional transmission interference, such as time division duplexing (TDD) [19] and wavelength division duplexing (WDD) [16], [29]. However, TDD requires strict time-slot synchronization and guard intervals, which increase system complexity and reduce transmission efficiency, while WDD relies on additional optical filters and multiple wavelength light sources, resulting in higher complexity, increased cost, and limited flexibility in resource allocation. To the best of our knowledge, interference cancellation schemes based on different frequency bands have not yet been investigated in the literature.

Distinct from that of conventional single-function systems, the performance optimization of ISAC systems is inherently a complex multi-objective optimization problem. Since the transmitted signals play distinct roles in communication and sensing tasks, an inevitable performance trade-off exists between the two when sharing spectrum resources and hardware platforms. Regarding unified performance metric design, existing works such as [30], [31], [32] have established foundational evaluation frameworks for ISAC systems. Although unified performance metrics for ISAC systems have jointly evaluated communication and sensing from various perspectives, these metrics are not directly applicable to RO-ISAC systems due to their unique retroreflective channel characteristics [9], [33] and signal coupling mechanisms. RO-ISAC systems currently lack a unified performance metric capable of simultaneously measuring communication quality of service (QoS) and sensing performance and reflecting the tight coupling relationship between them, which restricts system optimization. To address this deficiency, this work aims to bridge the gap by proposing a unified performance metric and a corresponding optimization framework. This approach enables dynamic resource balancing to jointly meet the dual requirements of high-performance communication and high-precision sensing.

In this paper, we propose and experimentally demonstrate a novel bidirectional RO-ISAC system, where clipped mCAP based subband division duplexing (SDD), interference cancellation and unified performance metric design are investigated. Compared with WDD, the SDD-based scheme emphasizes system simplicity and flexible resource allocation between communication and sensing. The comparison of transmission schemes is shown in Table I. The key contributions are summarized as follows:

- A SDD scheme based on clipped mCAP is first introduced into a bidirectional RO-ISAC system. By transmitting uplink and downlink signals over distinct frequency subbands, the proposed scheme enables flexible subband allocation for bidirectional links. Under this architecture, the downlink reflected and the uplink signals are detected by the same photodetector (PD), and the mixed signals are asynchronously superimposed in the time domain. Although the uplink communication signal can be effectively extracted from the mixed signals by leveraging the matched-filtering properties of mCAP, the downlink sensing process remains impaired by interference arising from the uplink signal.
- To mitigate the interference of the uplink signal on the reflected downlink signal, an interference cancellation method is proposed to enhance sensing accuracy, thereby enabling simultaneous downlink communication and sensing. Furthermore, by appropriately adjusting the clipping ratio (CR), a trade-off between downlink communication and sensing performance can be achieved, while the uplink bit error rate (BER) is simultaneously optimized.
- A unified performance metric, namely the joint communication-sensing outage probability (JCSOP), is further proposed to jointly optimize downlink communication and sensing performance. Based on this metric, the optimal CR can be identified to simultaneously meet communication and sensing requirements while achieving the minimum JCSOP.
- Through extensive experimental evaluation of the proposed clipped mCAP-based bidirectional RO-ISAC system, results show that downlink communication and sensing signals can effectively coexist without mutual interference in the proof-of-concept setup. This verifies

TABLE I
COMPARISON OF TRANSMISSION SCHEMES.

Reference	Year	Transmission mode	Waveform	Duplexing	Cons	Pros
[9]	2024	Downlink-only	OFDM	-	Unidirectional transmission only	-
[19]	2025	Bidirection	Clipped OFDM	TDD	Half-duplex transmission only	No interference and low hardware cost
[16]	2025	Bidirection	Hybrid PAM and OFDM	WDD	Additional optical filters, limited system flexibility and higher complexity	Full-duplex transmission and strong channel isolation
[17]	2025	Downlink-only	OFDM-MLS	-	Unidirectional transmission only	-
[18]	2026	Downlink-only	OFDM-MLS-CIM	-	Unidirectional transmission only	-
This work	2026	Bidirection	Clipped mCAP	SDD	Limited per-link bandwidth	Full-duplex transmission, low implementation complexity and flexible subband allocation

the robust potential of the proposed clipped mCAP based SDD scheme in practical bidirectional scenarios.

II. PRINCIPLE

In this section, the principle of the proposed bidirectional RO-ISAC based on clipped mCAP is presented, followed by a detailed discussion of SDD, sensing processing, and interference cancellation. Moreover, the frequently used notations are summarized in Table II.

A. System Principle

Fig. 1 illustrates the schematic diagram of a bidirectional RO-ISAC system using the proposed clipped mCAP based SDD scheme. In the RO-ISAC downlink device, the downlink input bits are first used to perform m_d-CAP subband modulation to generate a real-valued m_d-CAP waveform, where m_d is the number of downlink subbands. The downlink m_d subbands occupy the first to the m_d-th subbands among the m ($m \geq 2$ and $m > m_\mathrm{d}$) subbands and the number of downlink subbands can be flexibly configured. The principle of mCAP modulation with clipping is depicted in the inset (b) of Fig. 1. For mCAP modulation, the m groups of input data streams are independently mapped to M-quadrature amplitude modulation (M-QAM) constellation symbols. After upsampling, the mapped symbols are separated into real and imaginary components, which are filtered by the in-phase and quadrature filters, respectively. The two filters constitute a Hilbert pair and are time-orthogonal. The impulse responses of the in-phase and quadrature filters corresponding to the i-th ($i = 1, \cdots, m$) subband can be respectively expressed as [25]

$$f_i^\mathrm{I}(t) = g(t)\cos(2\pi f_{c,i}t), \tag{1}$$

$$f_i^\mathrm{Q}(t) = g(t)\sin(2\pi f_{c,i}t), \tag{2}$$

where $g(t)$ is the square-root raised cosine (SRRC) pulse, and $f_{c,i}$ represents the center frequency of the i-th subband. Since the downlink and uplink channels occupy different frequency subbands, the corresponding values of $f_{c,i}$ are different. The center frequency of the k-th ($k \in 1, \cdots, m_\mathrm{d}$) downlink subband is expressed by

$$f_{c,k}^\mathrm{d} = \frac{(1+\alpha)(2k-1)}{2T_{sub}^\mathrm{d}}, \tag{3}$$

where α is the roll-off factor of SRRC, and T_{sub}^d denotes downlink subband symbol period. Moreover, the bandwidths of the downlink and uplink signals can be flexibly configured and different bandwidth values are adopted in this work. The downlink signal bandwidth can be written as

$$B_\mathrm{D} = R_s^\mathrm{d}(1+\alpha) = \frac{1}{T^\mathrm{d}}(1+\alpha), \tag{4}$$

where R_s^d is the downlink system-level baud rate and T^d is downlink symbol period, satisfying $T^\mathrm{d} = m_\mathrm{d}T_{sub}^\mathrm{d}$.

Subsequently, the outputs of the filter pairs are subtracted to generate multiple independent subband signals, and the first m_d subband signals are then combined to generate the downlink m_d-CAP subband signal. To reduce the PAPR, the resultant subband signal is clipped with a certain CR. The digitally generated signal is converted into an analog electrical signal by a digital-to-analog (D/A) converter. After the addition of a direct-current (DC) bias, the resulting real-valued and non-negative downlink clipped m_d-CAP subband signal is employed to drive the LD transmitter. In the RO-ISAC uplink device, the downlink optical signal is detected by a PD and converted into an electrical signal, based on which the downlink received signal is expressed as

$$y_\mathrm{d}(t) = h_\mathrm{d}x_\mathrm{d}(t) + n(t), \tag{5}$$

where $x_\mathrm{d}(t)$ denotes the downlink transmitted signal, h_d is the line-of-sight (LOS) channel gain of the downlink communication module and $n(t)$ is the additive noise. Next, analog-to-digital conversion (A/D), time synchronization and m_d-CAP subband demodulation are successively executed to obtain the downlink output bits. The principle of mCAP demodulation is depicted in the inset (c) of Fig. 1. For m_d-CAP subband demodulation, the received signal after synchronization is passed through matched filter pairs corresponding to the m_d downlink subbands, thereby separately recovering the real and imaginary components of each subband. Finally, for each subband after the combination of real and imaginary components, downsampling, subband frequency-domain equalization (FDE) and M-QAM de-mapper are successively performed to finish signal demodulation.

As shown in Fig. 1, a CCR is integrated into the RO-ISAC uplink device to retro-reflect the received downlink optical signal back to the RO-ISAC downlink device along the same path, enabling simultaneous communication and

TABLE II
SUMMARY OF MAIN NOTATIONS

Symbol	Description	Symbol	Description
m	Number of subbands	$m_{\rm d}/m_{\rm u}$	Number of downlink/uplink subbands
M	constellation order	$f_{c,i}$	Center frequency of the i-th subband
$f^{\rm d}_{c,k}/f^{\rm u}_{c,k}$	Center frequency of the k-th downlink/uplink subband	α	Roll-off factor of SRRC
$T^{\rm d}_{sub}/T^{\rm u}_{sub}$	Downlink/Uplink subband symbol period.	$T^{\rm d}/T^{\rm u}$	Downlink/Uplink symbol period
$R^{\rm d}_s/R^{\rm u}_s$	Downlink/Uplink system-level baud rate	$B_{\rm D}/B_{\rm U}$	Downlink/Uplink signal bandwidth
$h_{\rm d}/h_{\rm u}/h_{\rm s}$	LOS channel gain of the downlink/uplink/sensing module	$L_s/L/D$	Recessed length/ length/diameter of the CCR
τ	Transmission timing offset between the uplink and downlink	λ	Upsampling ratio
L_w	Time-domain window length used for cross-correlation	c	Light speed
d_s	Actual distance between the downlink and uplink devices	S	A/D sampling rate in the downlink
$Signal_t/Signal_r$	Uplink transmitted/received signal	${\rm BER_c}/{\rm RMSE_s}$	Communication BER/Ranging error
${\rm BER_{th}}/{\rm RMSE_{th}}$	Maximum acceptable communication BER/ranging RMSE	$N_{\rm F}$	FFT/IFFT size
N	Number of sampling points in one complete period	$N_{\rm CP}$	CP length
f_s	AWG sampling rate for the downlink	-	

sensing. The diagram of the CCR model is depicted in the inset (a) of Fig. 1, where the recessed length, the length, and the diameter of the CCR are represented by L_s, L and D, respectively. The RO-ISAC downlink device is equipped with a PD to receive the downlink reflected signal for distance measurement, as detailed in the following subsection. Moreover, the RO-ISAC uplink device also integrates uplink transmission to achieve bidirectional ISAC. The uplink $m_{\rm u}$ subbands occupy the $(m_{\rm d}+1)$-th to the m-th subbands. The number of uplink subbands $m_{\rm u}$ can be flexibly configured, satisfying $m_{\rm u} = m - m_{\rm d}$. The center frequency of the k-th $(k \in 1, \cdots, m_{\rm u})$ uplink subband is expressed by

$$f^{\rm u}_{c,k} = B_{\rm D} + \frac{(1+\alpha)(2k-1)}{2T^{\rm u}_{sub}}, \tag{6}$$

where $T^{\rm u}_{sub}$ denotes uplink subband symbol period. The uplink signal bandwidth can be written as

$$B_{\rm U} = R^{\rm u}_s(1+\alpha) = \frac{1}{T^{\rm u}}(1+\alpha), \tag{7}$$

where $R^{\rm u}_s$ is the uplink system-level baud rate and $T^{\rm u}$ is the uplink symbol period, satisfying $T^{\rm u} = m_{\rm u}T^{\rm u}_{sub}$. The uplink optical signal is detected by a PD equipped in the downlink device. It is worth noting that the downlink reflected signal and the uplink communication signal are received by the same PD, resulting in a superimposed electrical signal consisting of both the downlink reflected signal $x_{\rm d}$ and the uplink signal $x_{\rm u}$, which is expressed by

$$y_{\rm m}(t) = h_{\rm u}x_{\rm u}(t-\tau) + h_{\rm s}x_{\rm d}(t) + n(t), \tag{8}$$

where $h_{\rm u}$ is the LOS channel gain of the uplink communication module, $h_{\rm s}$ is the LOS channel gain of the sensing module and τ denotes the transmission timing offset between the uplink and downlink links, which mainly arises from the fact that the uplink and downlink transmissions do not necessarily occur simultaneously. In addition, multipath reflections from walls and objects may significantly distort correlation sidelobes, particularly for clipped waveforms. This effect is not the focus of the current study and will be investigated in future work.

For $m_{\rm u}$-CAP subband demodulation, the mixed signals are demodulated using a matched filter corresponding to the uplink subbands, thereby enabling effective recovery of the uplink signal, while the downlink reflected signal is significantly suppressed due to spectral mismatch. This is mainly due to the SDD architecture, where the uplink and downlink signals occupy mutually orthogonal CAP subbands. For a detailed introduction to SDD, please refer to the following subsection. Consequently, the impact of the downlink reflected signal on uplink communication performance can be neglected, allowing reliable uplink communication to be achieved. However, for ranging based on time-domain correlation, the uplink signal is non-negligible interference and a transmission timing offset τ exists between the uplink and downlink signals, leading to elevated sidelobes and degraded ranging accuracy. Therefore, an interference cancellation scheme is proposed to suppress the interference between the downlink reflected and the uplink signals, as discussed in the following subsection. In addition, although Doppler effects may affect system performance in high-mobility scenarios, the proposed bidirectional RO-ISAC system primarily targets low-mobility short-range applications, with Doppler-related effects to be investigated in future work.

B. SDD

For frequency division duplex (FDD) based on OFDM, frequency partitioning is implemented at the subcarrier level, where different links are allocated to non-overlapping sets of orthogonal subcarriers, such that the downlink and uplink occupy spectrally separated frequency resources. However, the maintenance of subcarrier orthogonality relies heavily on accurate time synchronization and carrier frequency synchronization [34], [35]. In practical bidirectional communication scenarios, especially in RO-ISAC systems involving reflective links, the downlink reflected signal undergoes an additional reflection process, and the uplink and downlink transmissions are not necessarily strictly synchronized. As a result, the arrival time of the downlink reflected signal often exhibits a significant timing offset relative to the uplink signal. When the downlink reflected signal and the uplink signal are jointly received by the same PD, even if they are assigned to different subcarrier sets in the frequency domain, timing offsets exceeding the cyclic prefix (CP) duration can destroy subcarrier orthogonality, thereby introducing severe inter-carrier interference. This degradation adversely affects uplink communication performance. Consequently, in RO-ISAC scenarios, there is a

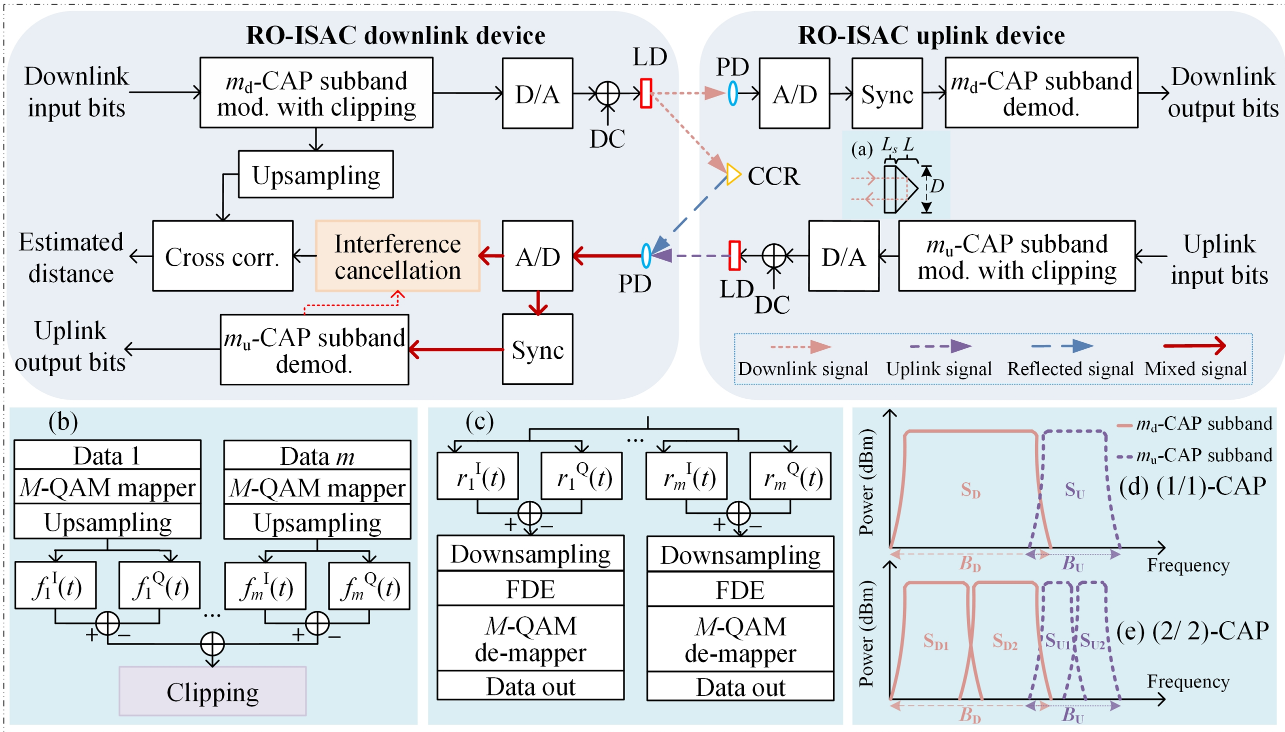

Fig. 1. Schematic diagram of the proposed bidirectional RO-ISAC system based on clipped mCAP. Insets: (a) CCR model, (b) mCAP modulation with clipping, (c) mCAP demodulation, (d) illustration of transmitted spectrum of (1/1)-CAP and (e) illustration of transmitted spectrum of (2/2)-CAP.

strong need for a multiplexing mechanism that is more robust to timing offset. Motivated by this consideration, this paper introduces a clipped mCAP based SDD scheme, where SDD is a subband-division-based frequency-domain duplexing scheme with a spectrum allocation mechanism different from that of conventional FDD.

Owing to the inherent multi-subband structure of mCAP modulation, SDD can be naturally implemented by allocating different subbands to the downlink and uplink. The fundamental principle of SDD is to divide the available system bandwidth into multiple mutually orthogonal subbands and flexibly allocate these subbands to different communication directions (downlink and uplink) or different functions (communication and sensing). Due to the subband processing structure based on filter groups, even if there is a timing offset, the spectral isolation between different subbands can still be maintained. Therefore, SDD has strong robustness against timing offsets and is particularly suitable for bidirectional RO-ISAC systems. Moreover, the number of subbands assigned to each transmission direction or function can be flexibly configured according to system requirements. Additionally, (m_d/m_u)-CAP denotes that m_d subbands and m_u subbands are allocated to the downlink and uplink, respectively. The insets (d) and (e) of Fig. 1 present the transmission spectrum of (1/1)-CAP and (2/2)-CAP, respectively.

Although clipping introduces spectral regrowth and may partially degrade subband isolation, its impact remains limited due to the rapid decay of out-of-band components and the reserved subband spacing in this work. Moreover, the digital signal processing (DSP) complexities of OFDM and mCAP are of the same order of magnitude, indicating that the proposed mCAP-based bidirectional RO-ISAC scheme does not introduce a significant complexity increase compared with conventional OFDM-based implementations.

C. Sensing Processing

Sensing directly reuses the downlink communication signal for ranging, requiring no additional spectrum resources while enabling efficient communication–sensing integration. In addition to downlink transmission and uplink reception, the RO-ISAC downlink device also includes sensing processing to finish ranging, as shown in Fig. 1. After the A/D conversion, the mixed signals received by the PD are further processed by an interference cancellation module to effectively suppress the interference from the uplink signal on the downlink reflected signal, thereby improving the ranging accuracy. Then, time-domain cross-correlation is performed between the received current signal and the upsampled downlink signal to estimate the time of flight and complete the distance estimation between the downlink and uplink devices. Let $x(n)$ and $y_\text{ref}(n)$ denote the upsampled time-domain samples of the original clipped m_d-CAP subband signal and the time-domain samples of the received current signal, respectively, where n is the sample index. The maximum likelihood time-of-flight estimate in samples is given by

$$\hat{\mathcal{T}} = \arg\max_{\mathcal{T}} \sum_{n=0}^{\lambda L_w} y_\text{ref}(n) x(n-\mathcal{T}), \tag{9}$$

where λ and L_w denote the upsampling ratio and the time-domain window length used for cross-correlation prior to upsampling, respectively. Accordingly, the distance is estimated as $\hat{d} = c\hat{\mathcal{T}}/2$ with c denoting the light speed, and hence the ranging root mean square error (RMSE) is then given by

$$\mathrm{RMSE} = \sqrt{\mathrm{mean}\left[(d_s - \hat{d})^2\right]}, \tag{10}$$

where d_s is the actual distance between the downlink and uplink devices. The ranging resolution and the maximum ranging distance can be expressed by $\triangle d = c/(2S)$ and $d_{\max} = c(\lambda L_w - 1)/(2S)$, respectively, where S denotes the A/D sampling rate in the downlink device.

D. Interference Cancellation

During the distance estimation process, ranging performance relies on accurate time-domain correlation characteristics, such as the peak position, sidelobe level, and the overall correlation shape. The presence of the uplink signal introduces an additional superimposed component in the received signal, whose power and correlation structure differ from those of the desired signal and therefore cannot be simply ignored, necessitating further interference modeling and cancellation.

Since the uplink received signal can be extracted from the mixed signals through a matched filter corresponding to the uplink subbands, the uplink communication is not affected by the downlink reflected signal and can be regarded as reliably recoverable. The uplink LOS channel gain is first estimated using the uplink transmitted signal $Signal_t$ and the received signal $Signal_r$, and is calculated as

$$\hat{h}_{\mathrm{u}} = \frac{Signal_r}{Signal_t}, \tag{11}$$

Based on the uplink output bits obtained after m_{u}-CAP subband demodulation, the uplink interference signal is reconstructed using the estimated uplink LOS channel gain. By subtracting the reconstructed interference from the mixed received signal, the estimated downlink reflected signal is obtained as

$$\hat{y}_{\mathrm{ref}}(t) = y_{\mathrm{m}}(t) - \hat{h}_{\mathrm{u}}\hat{x}_{\mathrm{u}}(t - \hat{\tau}). \tag{12}$$

where $\hat{x}_{\mathrm{u}}(t)$ is the estimate of the uplink transmitted signal, which is reconstructed from the uplink output bits after demodulation, and $\hat{\tau}$ is the estimated delay. Since the synchronized mixed signal has been aligned with the reconstructed uplink waveform, the uplink interference can be effectively suppressed through direct subtraction. Finally, the cross-correlation operation in Eq. (9) is applied to the downlink reflected signal to estimate the time of flight, and the distance estimate between the downlink and uplink devices can be obtained.

III. Unified Performance Metric Design

In ISAC systems, communication usually focuses on satisfying minimum QoS requirements, while sensing aims to meet minimum sensing accuracy constraints. Consequently, a single performance metric fails to capture overall system availability and is inadequate for comprehensive performance evaluation and joint communication–sensing resource optimization. By contrast, jointly considering communication and sensing directly affects subsequent system design and parameter optimization, and provides a comprehensive tool for overall system performance evaluation. Therefore, constructing a unified performance metric that can simultaneously reflect both communication and sensing capabilities is of critical importance. For RO-ISAC systems, this paper proposes a unified performance metric, named JCSOP.

Communication and sensing in the RO-ISAC system are carried out simultaneously, and system performance depends not only on communication quality but also on sensing accuracy. The proposed JCSOP is used to quantify the probability that at least one of the communication and sensing fails to meet its performance requirement, serving as a unified performance metric to evaluate overall system availability and reliability. A lower JCSOP indicates that the system simultaneously satisfies both communication and sensing requirements in most cases, implying high reliability, whereas a higher JCSOP reflects a greater likelihood of communication or sensing failures, indicating low overall system availability. In the threshold selection process, both BER and RMSE performance requirements should be taken into account. The objective of JCSOP is not to replace BER or RMSE, but to provide a unified criterion for system-level optimization and parameter optimization. This allows the system to maintain reliable communication while achieving high sensing accuracy, thereby enabling a proper trade-off between communication and sensing performance. The JCSOP may not conceal performance deterioration of communication BER and ranging RMSE. Assuming that $\mathrm{BER_c}$ denotes the communication BER and $\mathrm{RMSE_s}$ denotes the ranging error, the JCSOP is expressed as

$$P_{out} = 1 - \Pr(\mathrm{BER_c} \leq \mathrm{BER_{th}} \cap \mathrm{RMSE_s} \leq \mathrm{RMSE_{th}}), \tag{13}$$

where $\mathrm{BER_{th}}$ and $\mathrm{RMSE_{th}}$ are the maximum acceptable communication BER and ranging RMSE, respectively. By adjusting the CR, a trade-off between communication and sensing performance is established in the proposed RO-ISAC system. Utilizing the JCSOP as a unified performance metric to integrate BER and ranging RMSE evaluations, the optimal CR is identified to satisfy minimum performance requirements. This methodology yields a jointly optimized communication-sensing solution that, by attaining the minimum JCSOP, guarantees the overall reliability of the bidirectional system architecture.

IV. Results and Discussions

In this section, experiments are conducted to verify the performance of the proposed bidirectional RO-ISAC system using clipped mCAP based SDD scheme.

A. Experimental Setup

The experimental setup of the bidirectional RO-ISAC system is depicted in Fig. 2, where distinct frequency bands are allocated to the downlink and uplink transmissions, respectively. Both the downlink and uplink signals are generated offline using MATLAB and subsequently loaded into two ports of a four-channel arbitrary waveform generator (AWG, Suin TFG2934A), respectively, each operating at a sampling rate

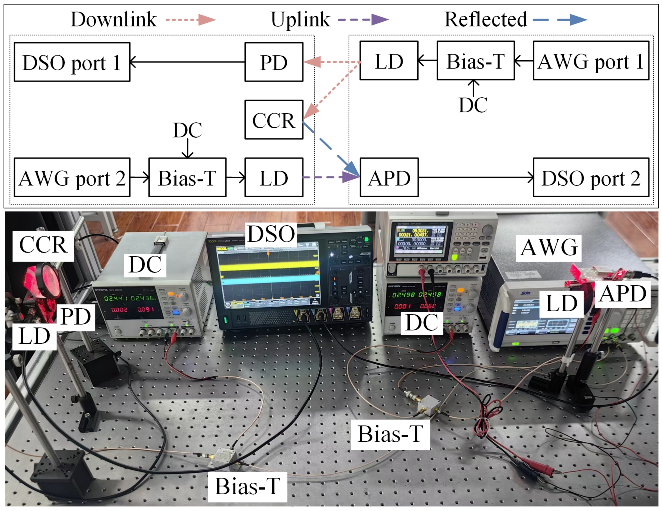

Fig. 2. Experimental setup of the bidirectional RO-ISAC system based on red LD. Insets: photo of the overall experimental testbed.

of 200 MSa/s. The downlink signal is first superimposed on a 2.5-V DC bias through a bias tee (Bias-T, Mini-Circuits ZFBT-6GW+) and then applied to drive a laser diode (LD, HL63603TG) with a wavelength of 638 nm. The uplink signal, on the other hand, is combined with a 2.4-V DC bias via another Bias-T and used to drive a separate but identical LD. The peak-to-peak voltages (Vpp) of the downlink and uplink signals are fixed at 500 mV and 400 mV, respectively. In the downlink, the red light is detected by a PD (Thorlabs PDA10A2), and the resulting signal is captured by a digital storage oscilloscope (DSO, Rigol DHO4404) at a sampling rate of 2 GSa/s for offline demodulation later via MATLAB. Moreover, a CCR is placed at the PD location to reflect the downlink beam back to the transmitter along the same path, and the reflected signal is received by an avalanche photodiode (APD, Hamamatsu C12702-12). In the uplink, the light is detected by the same APD. Therefore, the APD detects the mixed signals formed by the downlink reflected signal and uplink signal, which is then captured by the DSO at a sampling rate of 2 GSa/s for uplink demodulation. The experimental testbed photo is presented as the inset of Fig. 2.

TABLE III
EXPERIMENTAL PARAMETERS.

Parameter	Value
Number of subbands (m)	2/4
Roll-off factor (α)	0.125
FFT/IFFT size (N_{F})	256
CP length (N_{CP})	32
Downlink OFDM data subcarriers	36 (1st–36th)
Uplink OFDM data subcarriers	12 (37th–48th)
Constellation for downlink	8-QAM
Constellation for uplink	4-QAM
AWG sampling rate for downlink	200 MSa/s
AWG sampling rate for uplink	200 MSa/s
DSO sampling rate for downlink	2 GSa/s
DSO sampling rate for uplink	2 GSa/s
CCR diameter (D)	50 mm
CCR length (L)	35.7 mm
CCR recessed length (L_s)	6.3 mm

The overhead characteristics of OFDM and mCAP are fundamentally different, where OFDM incurs time-domain overhead while mCAP introduces frequency-domain overhead. To ensure a fair comparison, it is necessary to unify both OFDM and mCAP under the same efficiency metric, typically spectral efficiency (SE). The SEs of OFDM and mCAP with M-QAM are respectively expressed as $\eta_{\mathrm{OFDM}} = \log_2 M/(1+N_{\mathrm{CP}}/N_{\mathrm{F}})$ and $\eta_{m\mathrm{CAP}} = \log_2 M/(1+\alpha)$, where N_{CP} and N_{F} denote the CP length and the fast Fourier transform (FFT) size, respectively. Therefore, when $\alpha \approx N_{\mathrm{CP}}/N_{\mathrm{F}}$, the overheads introduced by OFDM and mCAP can be considered approximately equivalent. The experimental parameters are summarized in Table III. In the downlink modulation, the upsampling ratios of CAP and 2CAP are set to 8 and 16, respectively, yielding the same system-level baud rate R_s^{d} of 25 MBaud. Accordingly, the downlink data rate can be calculated as $25 \times \log_2 8 = 75$ Mbps. For performance comparison, OFDM is adopted as the benchmark scheme. The 1st to 36th OFDM data subcarriers are allocated to achieve the same data rate of $200 \times 36/(256+32) \times \log_2 8 = 75$ Mbps. In the uplink modulation, the upsampling ratios of CAP and 2CAP are set to 24 and 48, respectively, yielding the same system-level baud rate R_s^{u} of 8.33 MBaud. Consequently, the uplink data rate can be calculated as $8.33 \times \log_2 4 \approx 16.7$ Mbps. The 37th to 48th OFDM data subcarriers are allocated to achieve the same data rate of $200 \times 12/(256+32) \times \log_2 4 \approx 16.7$ Mbps. Moreover, the ranging resolution is calculated as $3 \times 10^8/(2 \times 2 \times 10^9) = 0.075$ m.

To realize asynchronous transmission between the uplink and downlink signals in the experiment, the uplink signal is delayed during sampling. To achieve precise timing offset $\triangle t$, a phase delay $\triangle \phi$ is introduced into the uplink signal, and the corresponding digital sample delay points are calculated as $k = \triangle \phi/(360^\circ/N)$, where N is the number of sampling points in one complete period and is fixed at 16384. The phase delay values are set to 0°, 0.7°, 1.4°, 2.1°, 2.8°, 3.5°, 4.2°, 4.9°, 5.6°, and 6.3°, where 0° denotes synchronous transmission between the uplink and downlink and a phase of 0.7° corresponds to a digital sample delay of approximately 32 points. The precise timing offset is then determined using the formula $\triangle t = \triangle \phi/(360^\circ f_s/N)$, where f_s is the AWG sampling rate for the downlink. In this way, the downlink reflected signal and uplink signal undergo asynchronous superposition in the time domain, thereby establishing an asynchronous state. In addition, although multi-objective evaluation methods such as weighted cost and Pareto front functions are important, they are beyond the scope of this work and will be considered in future studies.

B. Experimental Results

First, the PAPR comparison for downlink OFDM, CAP, and 2CAP signals is evaluated, where all schemes adopt the downlink parameter settings and are unclipped. The PAPR of all schemes is computed on a per-symbol basis. An OFDM symbol consists of an inverse FFT (IFFT) block and a CP, with a length of $N_{\mathrm{F}} + N_{\mathrm{CP}}$. As CAP and 2CAP do not inherently exhibit a block structure, their PAPR is calculated over an

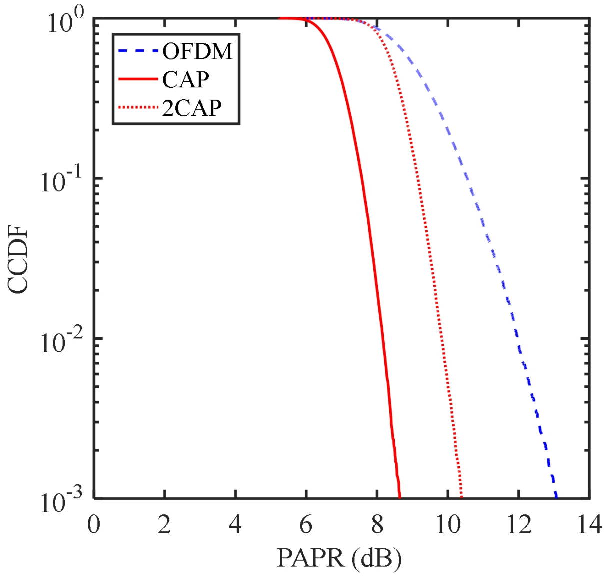

Fig. 3. PAPR comparison for different schemes.

equivalent symbol duration. Fig. 3 shows the complementary cumulative distribution function (CCDF) versus PAPR of different schemes. It can be seen that the CCDF decreases monotonically as the PAPR increases. Compared with OFDM and 2CAP, CAP exhibits the lowest PAPR, indicating the minimum susceptibility to nonlinear distortion. In addition, as the number of subbands increases from 1 to 2, the PAPR increases due to the superposition of multiple subband signals.

Fig. 4 shows the downlink and uplink transmitted spectrum for (1/1)-CAP and (2/2)-CAP. The uplink and downlink signals are separated in the frequency domain through SDD, where the downlink mainly occupies the low-frequency subbands, while the uplink is distributed over the high-frequency subbands. With different numbers of subbands, the spectral distribution and subband structure vary, and the subbands can be flexibly allocated to achieve finer spectral partitioning.

Fig. 5(a) shows the experimental uplink BER versus timing offset for OFDM and (1/1)-CAP at two CRs of 7 dB and 9 dB, with the transmission distance set to 90 cm. For clipped OFDM, when the timing offset is smaller than the CP length, the CP can effectively suppress the interference caused by timing misalignment, thereby preserving the orthogonality between the uplink and downlink subcarriers and enabling the system to achieve favorable BER performance. However, as the timing offset exceeds the CP length, the downlink reflected signal and the uplink signal partially overlap in the time domain, and the resulting timing misalignment destroys the inter-subcarrier orthogonality. Although the intra-subcarrier orthogonality can still be preserved, the inter-subcarrier interference is significantly enhanced, resulting in a degradation in the uplink BER performance. Moreover, when the timing offset approaches an integer multiple of the symbol duration, partial orthogonality is restored, and the BER performance may improve. Therefore, timing offset has a significant impact on the BER performance of the OFDM system, indicating a high sensitivity to timing misalignment, which further limits

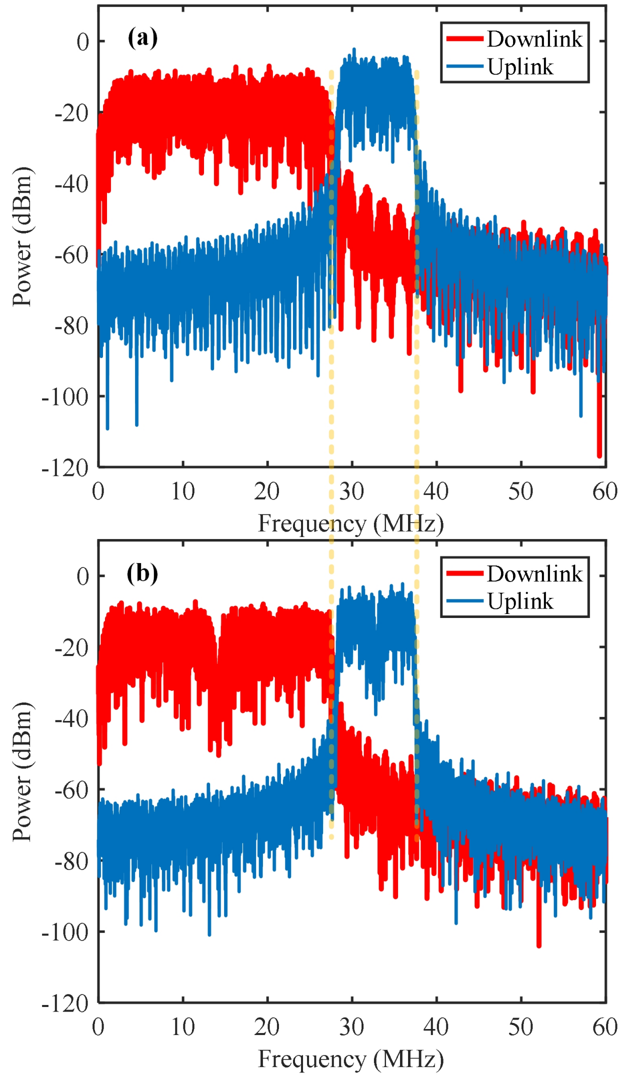

Fig. 4. The downlink and uplink transmitted spectrum for (a) (1/1)-CAP and (b) (2/2)-CAP.

its robustness in bidirectional RO-ISAC scenarios.

On the other hand, as shown in Fig. 5(a), clipped (1/1)-CAP is more robust in the asynchronous environment compared with clipped OFDM. Under different timing offsets, the BER performance of clipped (1/1)-CAP varies only slightly, demonstrating a high degree of insensitivity to timing offset. Specifically, for (1/1)-CAP with CRs of 7 dB and 9 dB, the uplink BER is maintained at around 2×10^{-4} and 2×10^{-3} respectively, unaffected by timing offset. This is mainly attributed to the use of mCAP matched filtering, where inter-subband interference is well confined by spectral shaping and out-of-band suppression, thereby effectively mitigating the inter-subband interference. Therefore, even in the presence of significant timing offsets between the uplink and downlink signals, the system can maintain inter-subband orthogonality, thereby demonstrating the superior robustness of clipped (1/1)-CAP in bidirectional RO-ISAC scenarios. Moreover, the CR has a significant impact on the BER performance for both OFDM and (1/1)-CAP, where the performance at CR = 7 dB is generally superior to that at CR = 9 dB. At the same CR,

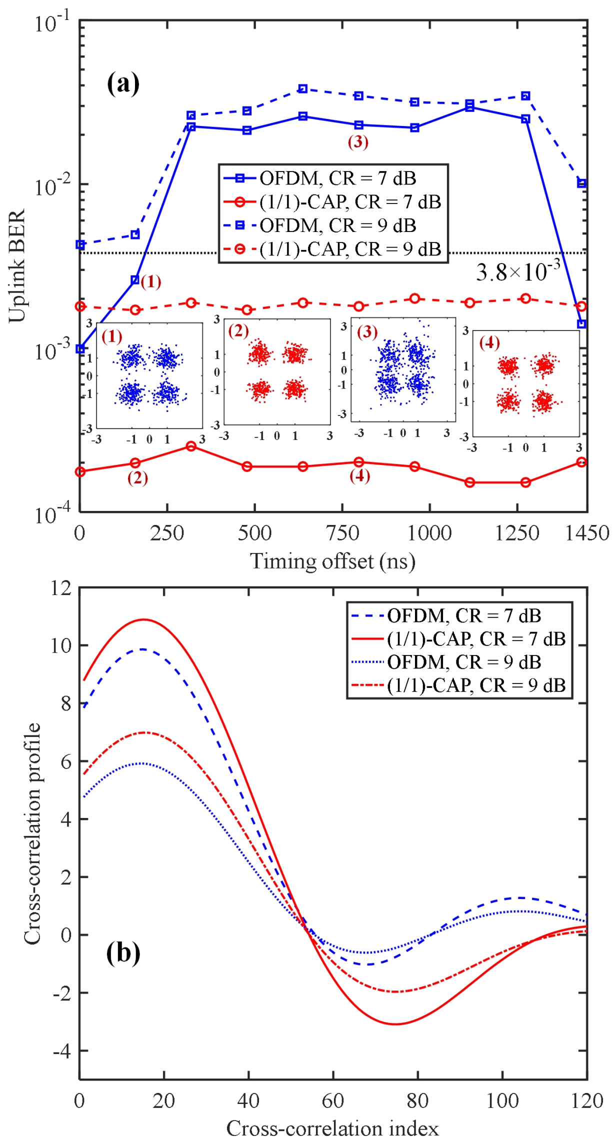

Fig. 5. (a) Experimental uplink BER vs. timing offset for OFDM and (1/1)-CAP under different CRs, and (b) cross-correlation performance comparison between OFDM and (1/1)-CAP under different CRs.

(1/1)-CAP outperforms OFDM in BER performance, which is primarily because the high-PAPR OFDM signals exceed the clipping threshold much more often than CAP signals, causing more frequent and severe signal clipping. To emulate a realistic asynchronous uplink-downlink transmission, the uplink time offset is set to 637 ns in the subsequent experiments. Additionally, the insets in Fig. 5(a) depict the received constellation diagrams of different schemes under various timing offsets at a CR of 7 dB.

Fig. 5(b) shows the cross-correlation performance comparison between OFDM and (1/1)-CAP under different CRs, with the transmission distance set to 105 cm and a cross-correlation window length of 3000. For both OFDM and (1/1)-CAP, the correlation peak at CR = 7 dB is higher than that at CR = 9 dB, which is because a lower CR makes the waveform more closely resemble a binary pulse signal, thereby enhancing the cross-correlation performance. Although (1/1)-CAP achieves a higher correlation peak than OFDM at the same CR, it suffers from significantly more severe negative sidelobes.

Subsequently, it is experimentally verified that clipping has different impacts on BER and sensing accuracy. Fig. 6(a) illustrates the communication downlink BER versus CR for OFDM, (1/1)-CAP and (2/2)-CAP under different distances. It is observed that the BER performance for all schemes is poor in the low CR region, attributed to severe signal clipping caused by an excessively low CR, which introduces significant non-linear distortion. Notably, an optimal CR exists for each scheme where the BER performance reaches its optimum, marking a balance point between clipping distortion and signal power. As the CR further increases into the high CR region, the BER performance degrades again, which occurs because while a higher CR reduces clipping distortion, it necessitates a decrease in effective signal power, resulting in substantial signal-to-noise ratio (SNR) degradation. The BER performance of (1/1)-CAP is superior to that of OFDM and (2/2)-CAP within the selected CR range. Particularly in the high CR region of 11-13 dB, the rise in BER for OFDM is significantly more pronounced than for the (1/1)-CAP and (2/2)-CAP schemes. Specifically, compared with other schemes, (1/1)-CAP achieves the optimal BER performance at a CR of 7 dB and a distance of 90 cm, reaching approximately 2×10^{-4}. Moreover, as the transmission distance increases from 90 cm to 105 cm, the signal quality of the considered schemes degrades, leading to an increase in BER. Fig. 6(b) illustrates the ranging RMSE versus CR for OFDM, (1/1)-CAP and (2/2)-CAP under different distances. It is interesting to observe that as the CR increases, the ranging RMSE of all schemes exhibits an upward trend. This is because that at small CRs, the waveform approaches a binary pulse-like shape, which improves its correlation properties and enhances ranging accuracy. As the CR increases, nonlinear distortion reduces the effective signal component, resulting in SNR degradation and increased ranging error. When the distance is 90 cm and compared with other schemes, clipped (1/1)-CAP achieves the lowest ranging RMSE, maintaining it below 3 cm. Meanwhile, clipped (2/2)-CAP exhibits a higher ranging RMSE than clipped (1/1)-CAP, as the increased number of subbands leads to a higher PAPR. In contrast, the clipped OFDM scheme demonstrates the highest ranging RMSE. For the considered schemes, the ranging RMSE at 105 cm is consistently higher than that at 90 cm, which is primarily attributed to the degradation of the SNR. According to Figs. 6(a) and (b), within different CR ranges, a pronounced trade-off exists between downlink communication reliability and sensing accuracy, and an appropriate selection of CR can achieve an optimal balance between acceptable communication and sensing performance.

Fig. 6(c) illustrates the communication uplink BER versus CR for OFDM, (1/1)-CAP and (2/2)-CAP under different distances. As the CR increases, the BER exhibits a trend of initially decreasing and then increasing. Compared with the other schemes, OFDM exhibits the poorest BER performance at the two considered distances, and even at the optimal CR, its BER remains consistently above the 7% forward error correction (FEC) coding limit of BER = 3.8×10^{-3}. When

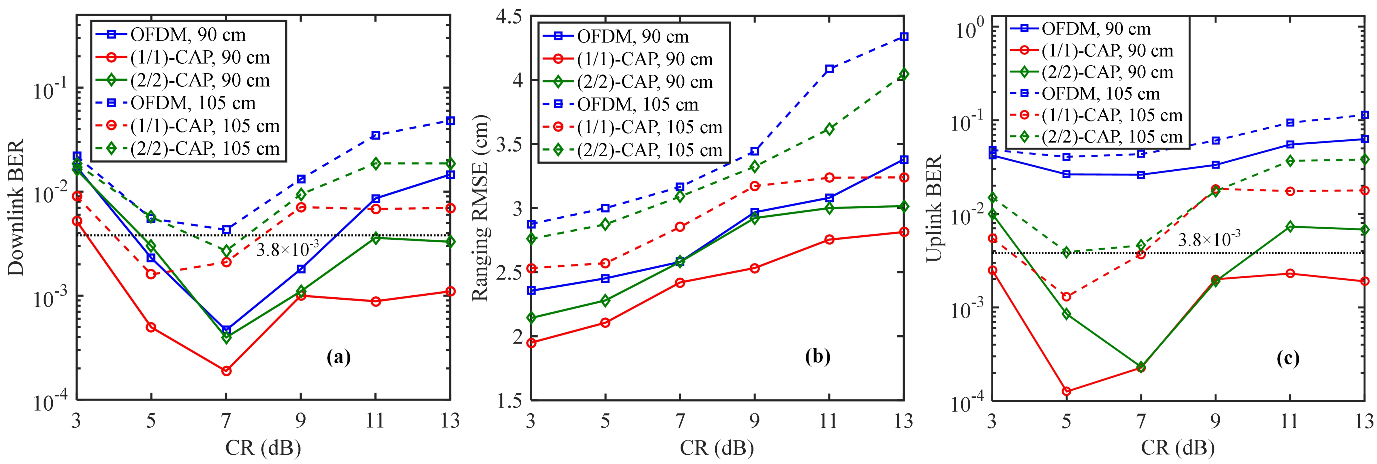

Fig. 6. (a) Communication downlink BER vs. CR for OFDM, (1/1)-CAP and (2/2)-CAP under different distances, (b) ranging RMSE vs. CR for OFDM, (1/1)-CAP and (2/2)-CAP under different distances and (c) communication uplink BER vs. CR for OFDM, (1/1)-CAP and (2/2)-CAP under different distances.

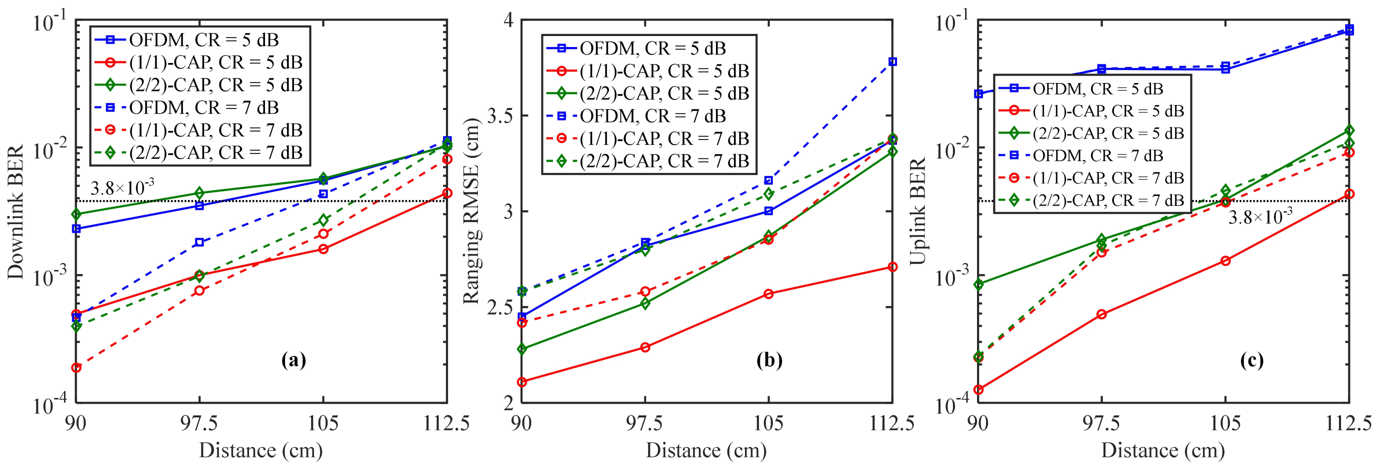

Fig. 7. (a) Communication downlink BER vs. distance for OFDM, (1/1)-CAP and (2/2)-CAP under different CRs, (b) ranging RMSE vs. distance for OFDM, (1/1)-CAP and (2/2)-CAP under different CRs and (c) communication uplink BER vs. distance for OFDM, (1/1)-CAP and (2/2)-CAP under different CRs.

the distance is 90 cm, the BER values of (1/1)-CAP remain below 3.8×10^{-3} over the considered CR range, while (2/2)-CAP can achieve a BER of 3.8×10^{-3} only within part of the CR range. As the distance increases, the BER values of all schemes increase accordingly. Therefore, the optimal uplink communication performance can be obtained by appropriately selecting the CR.

Fig. 7(a) illustrates the communication downlink BER versus distance for OFDM, (1/1)-CAP and (2/2)-CAP under different CRs. With the distance increasing from 90 cm to 112.5 cm, the BER curves of all schemes show an upward trend, indicating that communication quality degrades with increasing distance. At different distances, the optimal CR for (1/1)-CAP varies between 5 dB and 7 dB, while the optimal CR for other schemes remains consistently at 7 dB. Specifically, when satisfying the 7% FEC coding limit of BER = 3.8×10^{-3}, (1/1)-CAP with CR = 5 dB achieves the longest transmission distance among all schemes, reaching 111.4 cm, while OFDM achieves the shortest distance of 98.9 cm. Fig. 7(b) illustrates the ranging RMSE and the communication uplink BER versus distance for OFDM, (1/1)-CAP and (2/2)-CAP under different CRs. Increasing the transmission distance reduces the received SNR, thereby increasing the ranging RMSE and degrading sensing accuracy. As the distance increases from 90 cm to 112.5 cm, the ranging RMSE for all schemes at CR = 5 dB is consistently lower than at CR = 7 dB, further indicating that a smaller CR is beneficial for improving sensing accuracy. Specifically, at 112.5 cm, the OFDM scheme with CR = 7 dB exhibits a ranging RMSE approaching 3.8 cm, representing the maximum sensing error. In contrast, (1/1)-CAP achieves the lowest ranging RMSE, where particularly at CR = 5 dB, it is maintained between 2.1 cm and 2.8 cm across the entire distance range, demonstrating the highest accuracy and the slowest increase with distance. Therefore, combining the results from Figs. 7(a) and (b), it is evident that the clipped (1/1)-CAP scheme outperforms other schemes in terms of both communication and sensing performance. However, to simultaneously satisfy communication requirements and ensure an acceptable ranging RMSE, a trade-off in the selection of the CR is necessitated.

Fig. 7(c) illustrates the communication uplink BER versus distance for OFDM, (1/1)-CAP and (2/2)-CAP under different

TABLE IV
MAXIMUM DISTANCE COMPARISON UNDER BER AND RANGING RMSE THRESHOLDS.

Scheme	CR (dB)	Max. distance (cm) ($\mathrm{BER_{th}} = 3.8 \times 10^{-3}$) Downlink (Impr. over OFDM)	Max. distance (cm) ($\mathrm{BER_{th}} = 3.8 \times 10^{-3}$) Uplink (Impr. over (2/2)-CAP)	Max. distance (cm) ($\mathrm{RMSE_{th}} = 2.6$ cm, Impr. over OFDM)
OFDM	5	98.8	–	93.1
	7	104.0	–	90.7
(1/1)-CAP	5	111.4 (+12.8%)	111.8 (+6.8%)	106.6 (+14.5%)
	7	108.3 (+4.1%)	105.2 (+1.6%)	98.1 (+8.2%)
(2/2)-CAP	5	94.6 (-4.3%)	104.7	99.2 (+6.6%)
	7	106.9 (+2.8%)	103.5	90.7 (0%)

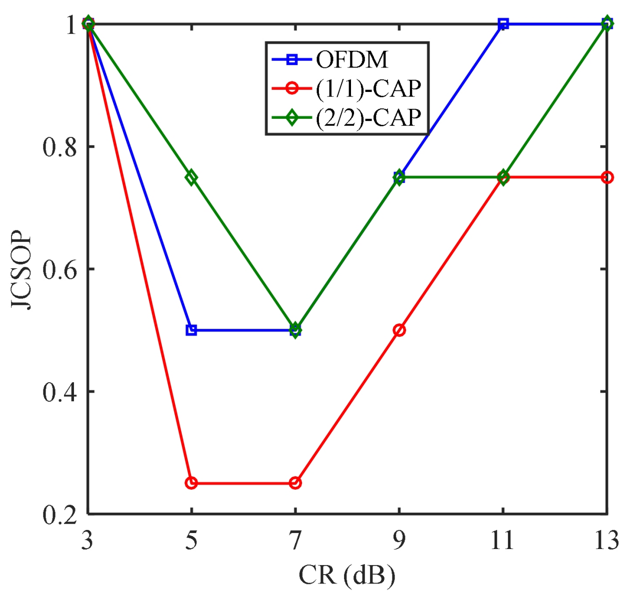

Fig. 8. JCSOP vs. CR for OFDM, (1/1)-CAP and (2/2)-CAP.

CRs. It can be observed that within the distance range of 90 cm to 112.5 cm, the BER of OFDM remains higher than 3.8×10^{-3} under different CR conditions. In contrast, the BER performance of both (1/1)-CAP and (2/2)-CAP schemes is significantly better than that of OFDM, indicating that (1/1)-CAP and (2/2)-CAP exhibit better interference robustness in this scenario. Furthermore, within the considered distance range, (1/1)-CAP achieves its best BER performance at CR = 5 dB, whereas for (2/2)-CAP, the optimal CR alternates between 5 dB and 7 dB depending on the transmission distance. Moreover, the maximum distance comparison under BER and ranging RMSE thresholds is shown in Table IV. These results indicate that (1/1)-CAP performs best in downlink communication, uplink communication, and ranging, demonstrating stronger communication robustness and better distance extension capability.

Since the CR plays a crucial role in the trade-off between clipping noise and signal power, Fig. 8 illustrates the JCSOP versus CR for OFDM, (1/1)-CAP and (2/2)-CAP, where the maximum acceptable communication BER $\mathrm{BER_{th}}$ and ranging RMSE $\mathrm{RMSE_{th}}$ are set to 3.8×10^{-3} and 3 cm, respectively. For a given CR, the BER and RMSE performances are evaluated at a set of discrete distance points. The JCSOP is obtained by counting the number of distance points where at least one performance metric exceeds the predefined thresholds and dividing it by the total number of distance points. It can be seen that all schemes exhibit a trend of initially decreasing and then increasing. This indicates that both excessively low and high CR values lead to an increased JCSOP, implying the existence of an optimal CR range. Within the optimal CR range, (1/1)-CAP achieves the lowest JCSOP compared with both OFDM and (2/2)-CAP, highlighting its advantage in terms of outage performance. Specifically, (1/1)-CAP achieves the lowest JCSOP of 0.25 within the CR range of 5 dB to 7 dB, significantly outperforming both OFDM and (2/2)-CAP. In comparison, OFDM exhibits a minimum JCSOP of 0.5 in the same range, while (2/2)-CAP only reaches this level at CR = 7 dB. This demonstrates that (1/1)-CAP provides the most robust link performance with a wider tolerance for CR variations. Moreover, when the CR exceeds the optimal point, the JCSOP for all schemes exhibits an upward trend, indicating that excessively high CR values lead to deteriorated system reliability, thereby making the selection of CR critical.

V. CONCLUSION

In this paper, we have proposed and investigated a novel bidirectional RO-ISAC system employing clipped mCAP based SDD scheme, where SDD is leveraged to allocate orthogonal frequency subbands for downlink and uplink transmissions. Within this architecture, the downlink reflected signal and the uplink signal arrive at the same PD with a time offset and are superimposed in the time domain. While the orthogonality provided by mCAP matched filtering facilitates the robust recovery of uplink data, the uplink signal poses a significant interference challenge to downlink sensing accuracy. Addressing the challenge of uplink-induced interference, we have proposed an interference cancellation scheme designed to restore downlink sensing precision. Adjustment of the CR serves as a pivotal mechanism to balance the trade-off between downlink communication and sensing performance, while concurrently optimizing the uplink BER performance. To address the challenge of quantifying the trade-off between communication and sensing, we have introduced a novel unified performance metric termed the JCSOP. Extensive hardware experiments definitively validate the feasibility and superiority of the proposed clipped mCAP based SDD scheme over conventional clipped OFDM counterparts in bidirectional RO-ISAC systems. Consequently, the proposed clipped mCAP based SDD scheme emerges as a highly promising solution for future bidirectional RO-ISAC deployments. Future work will explore adaptive clipping optimization, intelligent subband allocation, overlapped SDD for higher spectral efficiency, and extensions to multi-user RO-ISAC scenarios through the joint design of multi-user access and multi-target sensing.

References

[1] S. Walid, M. Bennis, and M. Chen, "A vision of 6G wireless systems: Applications, trends, technologies, and open research problems," *IEEE Network*, vol. 34, no. 3, pp. 134–142, May 2019.

[2] A. Kaushik, R. Singh, S. Dayarathna, R. Senanayake, M. D. Renzo, M. Dajer, H. Ji, Y. Kim, V. Sciancalepore, A. Zappone, and W. Shin, "Toward integrated sensing and communications for 6G: Key enabling technologies, standardization, and challenges," *IEEE Communications Standards Magazine*, vol. 8, no. 2, pp. 52–59, Jun 2024.

[3] Y. Wen, F. Yang, J. Song, and Z. Han, "Optical integrated sensing and communication: Architectures, potentials and challenges," *IEEE Internet of Things Magazine*, vol. 7, no. 4, pp. 68–74, Jul 2024.

[4] K. Kim, J. Kim, and J. Joung, "A survey on system configurations of integrated sensing and communication (ISAC) systems," in *International Conference on Information and Communication Technology Convergence (ICTC)*, Oct. 2022, pp. 1176–1178.

[5] M. Z. Chowdhury, M. T. Hossan, A. Islam, and Y. M. Jang, "A comparative survey of optical wireless technologies: Architectures and applications," *IEEE Access*, vol. 6, pp. 9819–9840, Jan 2018.

[6] X. Su, J. Song, Z. Liu, X. Guan, F. Yang, Y. Dong, H. Zhang, J. Wang, C. Pan, and X. Zhang, "Optical integrated sensing and communication: From theory to practice," *Tsinghua Science and Technology*, 2025.

[7] Y. Wen, F. Yang, J. Song, and Z. Han, "Pulse sequence sensing and pulse position modulation for optical integrated sensing and communication," *IEEE Communications Letters*, vol. 27, no. 6, pp. 1525–1529, Jun. 2023.

[8] H. Wang, Z. Zeng, C. Chen, B. Zhu, S. Shao, and M. Liu, "Retroreflective optical ISAC supporting 3D positioning in indoor environments," in *Asia Communications and Photonics Conference (ACP)*, Dec. 2024, pp. 1–5.

[9] Y. Cui, C. Chen, Y. Cai, Z. Zeng, M. Liu, J. Ye, S. Shao, and H. Haas, "Retroreflective optical ISAC using OFDM: Channel modeling and performance analysis," *Optics Letters*, vol. 49, no. 15, pp. 4214–4217, Aug. 2024.

[10] T. Chu, C. Chen, J. Ye, X. Xiong, S. Shao, Z. Zeng, D. Wang, F. Yang, G. Xu, and H. Haas, "Retroreflective optical ISAC for 6G: Architectures, technologies and future directions," *IEEE Vehicular Technology Magazine*, 2026.

[11] W. Wang, H. Wang, Z. Zeng, C. He, and C. Chen, "UAV-aided flying retroreflective optical ISAC with angle diversity transmitters," in *OptoElectronics and Communications Conference (OECC)*, Jul. 2025, pp. 1–4.

[12] Y. Cui, F. Liu, X. Jing, and J. Mu, "Integrating sensing and communications for ubiquitous IoT: Applications, trends, and challenges," *IEEE Network*, vol. 35, no. 5, pp. 158–167, Oct. 2021.

[13] X. Xiong, H. Wang, S. Shao, and C. Chen, "Hybrid MRR-assisted long-range SDMA for RO-ISAC systems in industry IoT applications," *Journal of Lightwave Technology*, vol. 44, no. 5, p. 1786–1799, Mar 2026.

[14] X. Wei, W. Yuan, K. Zhang, and F. Liu, "OTFS-assisted ISAC system: delay doppler channel estimation and SDR-based implementation," *IEEE Transactions on Mobile Computing*, vol. 24, no. 11, pp. 11 865–11 878, Nov 2025.

[15] A. Bemani, N. Ksairi, and M. Kountouris, "Integrated sensing and communications with affine frequency division multiplexing," *IEEE Wireless Communications Letters*, vol. 13, no. 5, pp. 1255–1259, May 2024.

[16] S. Chen, C. Chen, Z. Zeng, Y. Yang, and H. Haas, "Full-duplex RO-ISAC system: wavelength division duplexing and hybrid waveform design," *IEEE Photonics Technology Letters*, vol. 37, no. 15, pp. 869–872, Aug. 2025.

[17] J. Du, C. Chen, Z. Zeng, D. Wang, J. Ye, and J. Song, "Flexible waveform design for RO-ISAC based on OFDM-embedded maximum length sequence," *IEEE Communications Letters*, vol. 14, no. 10, pp. 3334–3338, Oct. 2025.

[18] W. Wang, C. Chen, H. Wang, Z. Zeng, D. Wang, and J. Ye, "Multiuser retroreflective optical ISAC: waveform design, joint sensing and multiple access," *Journal of Lightwave Technology*, vol. 44, no. 6, p. 2247–2255, Mar 2026.

[19] H. Wang, C. Chen, Z. Zeng, S. Shao, and H. Haas, "Bidirectional retroreflective optical ISAC using time division duplexing and clipped OFDM," *IEEE Photonics Technology Letters*, vol. 37, no. 10, pp. 587–590, May. 2025.

[20] Y. Nie, C. Chen, S. Savovic, Z. Wang, R. Min, X. You, Z. Zeng, and G. Shen, "0.5-bit/s/Hz fine-grained adaptive OFDM modulation for bandlimited underwater VLC," *Optics Express*, vol. 32, no. 3, pp. 4537–4552, Jan. 2024.

[21] M. Kim, W. Lee, and D.-H. Cho, "A novel PAPR reduction scheme for OFDM system based on deep learning," *IEEE Communications Letters*, vol. 22, no. 3, pp. 510–513, Mar. 2018.

[22] H. Ochiai and H. Imai, "Performance analysis of deliberately clipped OFDM signals," *IEEE Communications Letters*, vol. 50, no. 1, pp. 89–101, Jan. 2002.

[23] K. O. Akande, P. A. Haigh, and W. O. Popoola, "On the implementation of carrierless amplitude and phase modulation in visible light communication," *IEEE Access*, vol. 6, pp. 60 532–60 546, Oct. 2018.

[24] F.-M. Wu, C.-T. Lin, C.-C. Wei, C.-W. Chen, H.-T. Huang, and C.-H. Ho, "1.1-Gb/s white-LED-based visible light communication employing carrier-less amplitude and phase modulation," *IEEE Photonics Technology Letters*, vol. 24, no. 19, pp. 1730–1732, Oct. 2012.

[25] P. A. Haigh, S. T. Le, S. Zvanovec, Z. Ghassemlooy, P. Luo, T. Xu, P. Chvojka, T. Kanesan, E. Giacoumidis, P. Canyelles-Pericas, H. L. Minh, W. Popoola, S. Rajbhandari, I. Papakonstantinou, and I. Darwazeh, "Multi-band carrier-less amplitude and phase modulation for bandlimited visible light communications systems," *IEEE Wireless Communications*, vol. 22, no. 2, pp. 46–53, Apr. 2015.

[26] M. M. Merah, H. Guan, and L. Chassagne, "Performance optimization in multi-user multiband carrierless amplitude and phase modulation for visible light communication," in *Global LIFI Congress (GLC)*, Feb. 2018, pp. 1–4.

[27] Y. Nie, C. Chen, Z. Zeng, X. You, and G. Shen, "Multi-mode index modulation aided multi-band CAP with balanced pairwise coding for bandlimited VLC systems," *Journal of Lightwave Technology*, vol. 43, no. 5, p. 2053–2066, Mar 2025.

[28] Y. Nie, C. Chen, Z. Zeng, X. You, H. Haas, and G. Shen, "Interference mitigation for faster-than-Nyquist mCAP in bandlimited VLC: A low-complexity gapped index modulation approach," *Journal of Lightwave Technology*, vol. 43, no. 14, p. 6533–6546, Jul 2025.

[29] S. Chen, Z. Zeng, and C. Chen, "Experimental demonstration of multi-user full-duplex RO-ISAC system," in *Asia Communications and Photonics Conference (ACP)*, Dec. 2025.

[30] S. Wang, L. Chen, J. Zhou, Y. Chen, K. Han, and C. You, "Unified ISAC pareto boundary based on mutual information and minimum mean-square error estimation," *IEEE Transactions on Communications*, vol. 72, no. 11, pp. 6783–6795, Nov. 2024.

[31] F. Dong, F. Liu, Y. Cui, W. Wang, K. Han, and Z. Wang, "Sensing as a service in 6G perceptive networks: A unified framework for ISAC resource allocation," *IEEE Transactions on Wireless Communications*, vol. 22, no. 5, pp. 3522–3536, May. 2023.

[32] X. Gan, C. Huang, Z. Yang, X. Chen, J. He, and Z. Zhang, "Toward a unified analytical framework for ISAC fundamentals in cellular networks," in *IEEE 99th Vehicular Technology Conference (VTC-Spring)*, Sep. 2024, pp. 1–6.

[33] S. Shao, A. Salustri, A. Khreishah, C. Xu, and S. Ma, "R-VLCP: Channel modeling and simulation in retroreflective visible light communication and positioning systems," *IEEE Internet of Things Journal*, vol. 10, no. 13, pp. 11 429–11 439, Jul. 2023.

[34] J.-J. van de Beek, P. Borjesson, M.-L. Boucheret, D. Landstrom, J. Arenas, and P. Odling, "A time and frequency synchronization scheme for multiuser OFDM," *IEEE Journal on Selected Areas in Communications*, vol. 17, no. 11, pp. 1900–1914, Nov. 1999.

[35] Q. Huang, M. Ghogho, J. Wei, and P. Ciblat, "Practical timing and frequency synchronization for OFDM-based cooperative systems," *IEEE Transactions on Signal Processing*, vol. 58, no. 7, pp. 3706–3716, Jul. 2010.